PHYSICAL REVIEW FLUIDS **3**, 113901 (2018)

Editors' Suggestion

Control of flow around a low Reynolds number airfoil using longitudinal strips

Seunghyun Cho,[1] Jooha Kim,[2] and Haecheon Choi[1,3,*]

[1]*Department of Mechanical & Aerospace Engineering, Seoul National University, Seoul 08826, Korea*

[2]*School of Mechanical and Nuclear Engineering, UNIST, Ulsan 44919, Korea*

[3]*Institute of Advanced Machines and Design, Seoul National University, Seoul 08826, Korea*

(Received 4 July 2018; published 7 November 2018)

We suggest longitudinal strips attached to an airfoil surface as a new stall control device. Their effects on the stall characteristics and flow modifications are experimentally investigated. The airfoil considered is SD7003 and the Reynolds numbers are Re = 60 000 and 180 000 based on the chord length and freestream velocity. The drag and lift forces on the airfoil are measured by varying the angle of attack from $\alpha = 0^\circ$ to 16° with and without strips. The optimal strip configuration is determined using a response surface method. Without strip, abrupt stalls occur at $\alpha = 11^\circ$ and 12.5° for Re = 60 000 and 180 000, respectively, whereas broad stalls occur without much changing the stall angles by optimal strips. The lift coefficient and lift-to-drag ratio are significantly increased by the strips at post-stall angles of attack. A corner vortex is generated at each corner of strip near the leading edge. Clockwise and counterclockwise streamwise vortices are generated at the left- and right-facing corners, respectively, and they slowly move away from the corners while travelling downstream. These vortices provide additional momentum to the airfoil suction surface, resulting in fully attached flow above the strips and reattachment of flow above grooved surface. The longitudinal strips presented here are different from other devices such as the vortex generator, trip wire, burst control plate, and zigzag tapes used for the separation control of low Reynolds number airfoil, in that the strips are installed nearly on the whole airfoil surface but with their heights lower than the boundary layer thickness, and produce positive control effects at post-stall angles of attack but little affect the aerodynamic performance at prestall angles of attack.

DOI: 10.1103/PhysRevFluids.3.113901

I. INTRODUCTION

Unmanned aerial vehicles (UAVs) have a number of advantages over manned aircraft [1]: e.g., they can perform tasks in a dangerous environment where people cannot access; perform repetitive and tedious tasks that are difficult to perform with manned aircrafts; reduce labor costs for commercial use. Among UAVs, small UAVs, categorized as vehicles with wing span less than 6 m and mass less than 25 kg [2], have recently received much attention owing to their ability to perform various missions. These small UAVs run in a Reynolds number range between 15 000 and 500 000 [2]. In this range, laminar separation bubble forms on a wing surface and degrades the aerodynamic performance [3–5]. Thus, eliminating, reducing or delaying laminar separation bubble has been an important task, and SD series airfoils have been developed for this purpose [5]. However, laminar separation bubble still exists even for the SD series airfoils. As a result, at high angles of attack, stall occurs due to the burst of laminar separation bubble, which significantly reduces the aerodynamic

*choi@snu.ac.kr

performance [3]. Therefore, it is important to control flow separation at high angles of attack for improving the aerodynamic performance of low Reynolds number (Re $<$ 500 000) airfoils.

A number of active and passive devices have been developed to control flow separation for low Reynolds number airfoils [6]. Active devices such as plasma actuators [7–9], acoustic excitation [10], and periodic forcing [11] were effective to control flow separation. These active control devices were activated in post- or deep-stall regions, and increased the lift coefficient [8], or lift-to-drag ratio [7,9–11]. However, they require power expenditure and thus have a limitation in applying to small UAVs with limited energy capacity.

In this sense, passive devices may be appropriate to apply for small UAVs, because they do not require any external power to operate. Vortex generators [12–15], trip wires [16–18], burst control plate [19–21], and zigzag tapes [17,22,23] were investigated to enhance the aerodynamic performance of low Reynolds number airfoils (see, for a review, Tongsawang [24]). In particular, low profile vortex generators ($h/\delta \ll 1$) had low device drags and were installed upstream of the separation point to effectively control separation [25], where h is the height of vortex generator and δ is the boundary layer thickness. A low profile vortex generator with $h/c = 0.0016$ (c is the chord of the airfoil) was applied to an LA2573 airfoil at Re $=$ 235 000 [13], and reduced the drag by 38% at a low angle of attack of 4°. However, it had limitation in increasing the lift-to-drag ratio in a post-stall region [13]. Various studies were conducted for the purpose of separation control at high angles of attack using vortex generators with their large heights ($h/c = 0.024 \sim 0.04$), reporting delayed stall [12] or increased maximum lift coefficient [14,15]. However, those high profile vortex generators increased the drag at low angles of attack. Trip wires installed near or on the leading edge reduced the drag at low angles of attack [17,18] or eliminated lift hysteresis in a post-stall region [16], but they did not properly control stall. A burst control plate with its height of $h/c = 0.005$ located near leading edge was shown to delay stall and increase the lift coefficient in a post-stall region [19–21]. However, it reduced the lift and increased the drag at low angles of attack [20]. Several types of zigzag tapes ($h/c = 0.00067 \sim 0.0039$) installed along the spanwise direction of low Reynolds number airfoils (E374 [17]; E387, FX 63–137, S822, S834, SD2030, and SH3055 [22]) decreased the drag coefficient at low angles of attack, but the stall control effect was negligible [22]. Zigzag tapes ($h/c = 0.0013$) were also tested on a NACA 63_3–618 airfoil at low Reynolds number range (Re $=$ 64 200 and 137 000), and they increased the lift-to-drag ratio at low angles of attack but were not effective for stall control [23].

Most of the passive control devices described above were applied along the spanwise direction at a specific streamwise location and reduced the drag or increased the lift at some specific angles of attack. The performance of these control devices depended on the angle of attack and provided negative effects at some other angles of attack. In this regard, we suggest longitudinal strips with low profile heights ($h/\delta \ll 1$) as a new stall control device. They are attached to almost whole surface of the SD7003 airfoil. We directly measure the lift and drag forces at wide angles of attack for the cases with and without the strips, conduct surface-oil visualization, and measure the surface pressure and velocity field. The optimal configuration of the strips (i.e., height and width of each strip, and spacing between adjacent strips) is obtained using a response surface method at a post-stall angle of attack of 12°. We show in this paper that these longitudinal strips effectively control the stall but little affect the aerodynamic performance at low angles of attack.

II. EXPERIMENTAL SETUP

Figure 1 shows the schematic diagram of the experiment setup. The experiment is conducted in a closed-type wind tunnel whose test section is 0.9 m wide and 0.9 m high. The x, y, and z denote the streamwise, vertical, and spanwise directions, respectively. The blockage ratio of the model to the wind-tunnel test section is 6.1% at the angle of attack of 16° that is smaller than the minimum blockage ratio recommended to avoid disturbances from the wind-tunnel wall [26]. To reduce the wind-tunnel wall and wing-tip effects, end plates (700 mm long, 800 mm wide, and 20 mm thick) are installed near the tips of the airfoil. The gap between the end plate and airfoil is kept within 1 mm,

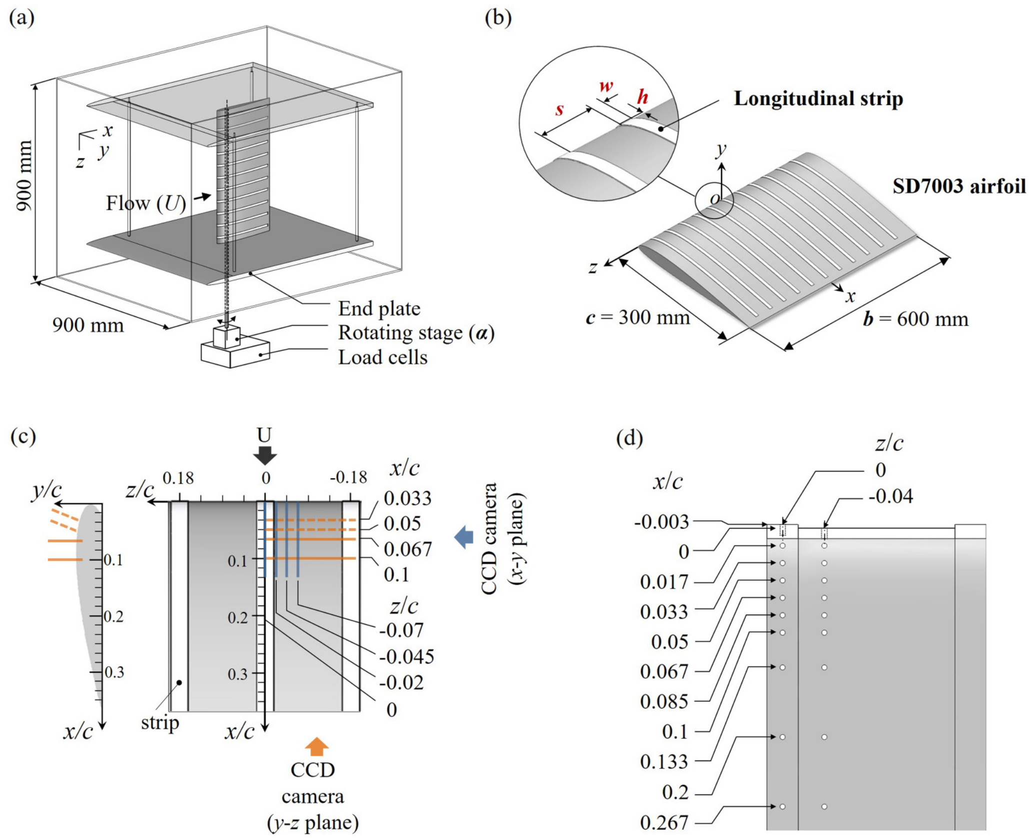

FIG. 1. Schematic diagram of the experimental setup: (a) overall view; (b) airfoil and longitudinal strips; (c) two-dimensional planes for PIV measurements; (d) surface pressure measurement locations.

and thus the leakage flow in the gap little affects the measured forces [27]. The airfoil is SD7003 with a span of $b = 600$ mm and a chord length of $c = 300$ mm. Its aspect ratio is $AR = b/c = 2$. End plates with this AR allow us to measure accurate lift and drag forces [28]. The strips are attached to both the pressure and suction surfaces of the airfoil except very near the trailing edge, and their geometric configuration has three parameters; height h, width w, and spacing between the adjacent strips s [Fig. 1(b)].

With strips, we want to maximize the lift coefficient at a post-stall angle of attack ($\alpha = 12^\circ$; see below) for Re = 60 000. To determine the optimal configuration of strips, we use a second-order response surface method [29–31] with three independent variables (h, w, s). The parameter domain consists of $0 \leqslant h/c \leqslant 0.005$, $0.0167 \leqslant w/c \leqslant 0.05$, and $0.06 \leqslant s/c \leqslant 0.267$, where the case of $h = 0$ denotes no strip. The boundary layer thickness near the leading edge ($x/c \approx 0.02$) of the SD7003 is $\delta/c \approx 0.006$ at a prestall angle of attack of 11° [32], so the strip height considered is smaller than the boundary layer thickness near the leading edge. Previously, longitudinal grooves were attached to airfoils for the purpose of drag reduction [33,34] or lift increase [35] at low angles of attack. These grooves had the sizes of $h/c = 0.00015 \sim 0.1$, $s/c = 0.00015 \sim 0.21$, and $h/s = 0.48 \sim 1.0$, where h is the depth of the grooves. The ratio of height (or depth) to spacing used for longitudinal grooves were much larger than those of the present strips ($h/s = 0.011 \sim 0.083$). Since these longitudinal grooves were not effective for stall control [35], we did not consider those sizes of longitudinal grooves in the present study. The Reynolds numbers based on the freestream velocity (U) and chord length are Re = 60 000 and 180 000. The uniformities of the mean streamwise velocity and turbulence intensity are both within 0.5% at the freestream velocity of $3 \sim 10$ m/s. The angle of attack is adjusted from 0° to 16° through the rotating stage with a resolution of 0.5° [Fig. 1(a)]. The lift (L) and drag (D) forces are measured using two load cells (LCB03, AND) with a measurement uncertainty of $\pm 2.1\%$ [36]. Resolutions of these load cells are both 0.003N with maximum capacities of 30N. The voltage is amplified by a signal conditioning amplifier (2310B, Vishay micro-Measurements), and digitized by an A/D converter (PXI-6259, National Instruments Co.). The digital signals are transferred to a computer. After they reach a steady state, the signals are sampled during 40 s at a rate of 10 kHz to obtain mean drag and lift forces. Solid blockage, wake blockage, and streamline curvature corrections are then applied to those values to obtain the force coefficients [37], where the lift and drag coefficients are defined as $C_L = L/(0.5\rho U^2 A)$ and $C_D = D/(0.5\rho U^2 A)$, respectively, $\rho(=1.21\,\mathrm{kg/m^3})$ is the density of air, and A is the planform area of the airfoil.

A mixture of oil and white ink is used to visualize the flow on the airfoil and strip surfaces. For the purpose of visualization, the airfoil is reinstalled horizontally in the middle of the test section; otherwise, the oil moves downward due to the gravitational force when the airfoil is installed vertically as in Fig. 1(a). The oil-flow pattern on the airfoil surface is photographed after the oil movement stops. Instantaneous flow fields are measured using PIV (particle image velocimetry) at four spanwise (x-y planes at $z/c = 0, -0.02, -0.045$, and -0.07) and streamwise (y-z planes at $x/c = 0.033, 0.05, 0.067$, and 0.1) locations [see Fig. 1(c)]. Here, at $x/c = 0.033$ and 0.05, we adjust the laser sheet to be nearly perpendicular to the airfoil surface to better measure near-surface flow; otherwise, the airfoil shades the near surface region at $x/c = 0.033$ and 0.05. The PIV system consists of a fog generator (F2010, SAFEX), an Nd:Yag laser (Dual Power 135-15, Litron laser), a CCD camera (VH-4M, Vieworks) with a 2048 pixel $\times$ 2048 pixel resolution, and a timing hub (IDT USB Timing Hub XS-TH, Integrated Design Tools). Particles about 1 μm in diameter are injected through the fog generator and illuminated by the laser sheet. Images are acquired by the CCD camera, and the time interval between two images is $\Delta t = 10\,\mu$s. A recursive cross-correlation is used to obtain flow fields, in which the interrogation window size is refined from 64×64 to 16×16 [38]. The interrogation window overlap ratio is 50%, and the spatial resolutions in x-y and y-z planes are 0.117 mm ($3.9 \times 10^{-4}c$) and 0.162 mm ($5.4 \times 10^{-4}c$), respectively. To identify and remove spurious vectors, both normalized median filter [39] and pixel shift limit are used. Spurious vectors eliminated by these methods are replaced by linear interpolation of surrounding 3×3 set of vectors. About one thousand instantaneous flow fields are averaged to obtain the mean flow field.

Pressures are measured on the suction (SS) and pressure (PS) surfaces of the airfoil. They are measured at the center of strip ($z/c = 0$) and a spanwise location in between strips ($z/c = -0.04$) [Fig. 1(d)]. Ten and six pressure tabs are located on SS and PS, respectively. The pressure tabs are connected to a manometer (MKS 220DD, MKS instruments) via scannivalve. The manometer has a measurement range of 0 to 1 torr, with a maximum uncertainty of 0.15%. At each pressure tab, the signals are transferred to the computer via an A/D converter (NI PCI-6251, National Instruments Co.), and sampled during 40 s at the rate of 10 kHz after they reach a steady state. The surface pressure coefficient is defined as $C_P = (P - P_\infty)/(0.5\rho U^2)$, where P and P_∞ are the surface and freestream pressures, respectively.

Figure 2 shows the variations of the lift and drag coefficients with the angle of attack, together with those from previous studies [5,32,37]. The stall occurs at $\alpha = 11^\circ$ and the maximum lift coefficient is 1.07. The lift and drag coefficients rapidly decreases and increases, respectively, after stall. The present force coefficients before stall agree very well with those by Selig *et al.* [5,37] and Galbraith and Visbal [32]. Since SD7003 airfoil is cambered, the lift coefficient at $\alpha = 0^\circ$ is not zero [37]. After stall, the lift coefficient does not match with that of Galbraith and Visbal [32] obtained by numerical simulation, but the stall angle of attack is same as theirs ($\alpha = 11^\circ$). The optimal configuration of strips for the lift force enhancement is searched for at a post-stall angle of attack of 12°.

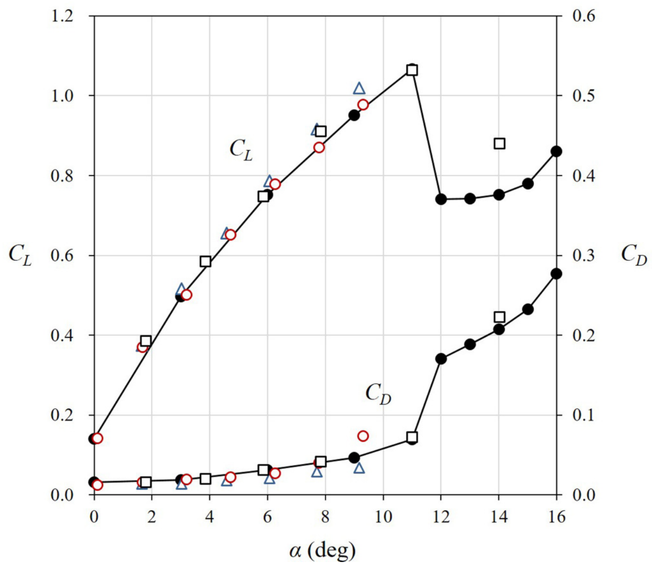

FIG. 2. Variations of the lift and drag coefficients with the angle of attack (α): ●, present (Re = 60 000); ○, Selig *et al.* [5] (Re = 60 000); □, Galbraith and Visbal [32] (Re = 60 000); △, Selig *et al.* [37] (Re = 61 400).

III. RESULTS

A. Lift and drag coefficients

Figure 3 shows the contours of the lift coefficient with the strip parameters ($h/c,\ w/c,\ s/c$) using a response surface method at a post-stall angle of attack of 12° of Re = 60 000, where the reliability

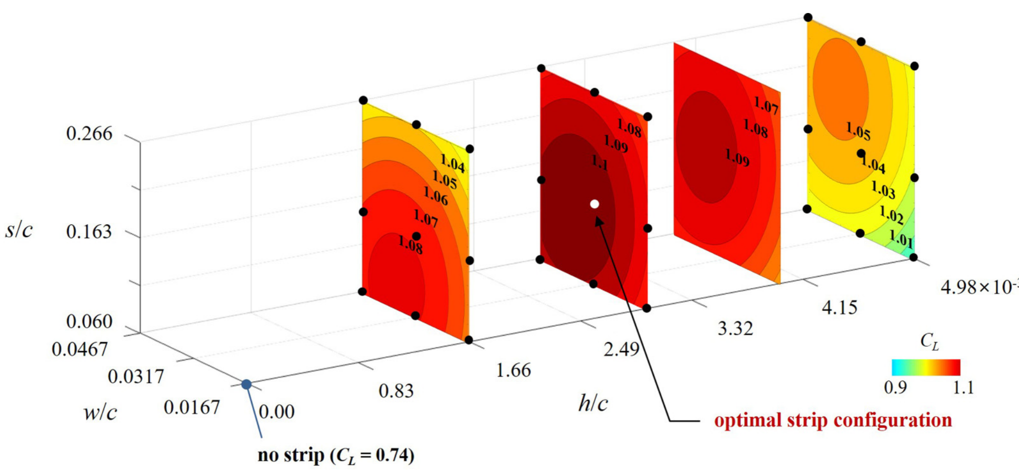

FIG. 3. Contours of the lift coefficient with the strip parameters ($h,\ w,\ s$) at a post-stall angle of attack ($\alpha = 12^{\circ}$) using a response surface method. Thin solid lines denote the contour levels from $C_L = 0.9$ to 1.1 by increments of 0.01. The force measurement locations are denoted as (black and white) solid circles in this figure. The response surface method provides an optimal strip configuration where no measurement is conducted, and thus we take the strip configuration closest to the one suggested as the optimal strips (denoted as white dot).

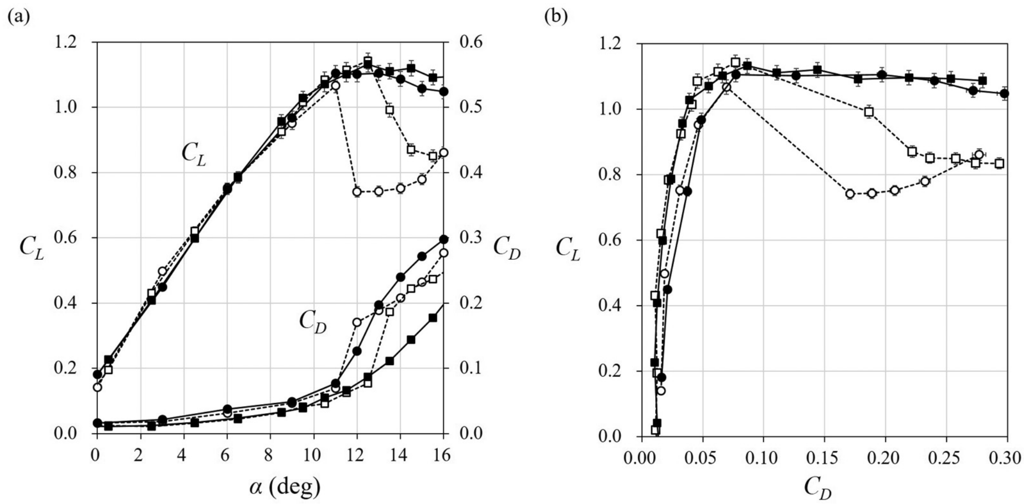

FIG. 4. Variations of the force coefficients and drag polar with the angle of attack by strips: (a) C_L and C_D; (b) drag polar. ··○··, No strip (Re = 60 000); —●—, optimal strips (Re = 60 000); ··□··, no strip (Re = 180 000); —■—, optimal strips (Re = 180 000). Here, the optimal strip configuration is $h/c = 0.003$, $w/c = 0.03$, and $s/c = 0.15$.

factor of the second-order response surface model is $R^2 = 99.6\%$. The maximum lift coefficient is $C_L \approx 1.11$ for the optimal strip configuration of $(h/c, w/c, s/c) = (0.003, 0.03, 0.15)$. The amount of lift coefficient increase is 50% as compared to that without strip ($C_L = 0.74$). Note that the lift coefficient slowly changes with respect to the strip height because it is still smaller than the boundary layer thickness near the leading edge of the airfoil [32]. The optimal strip configuration for $\alpha = 13^\circ$ is also the same as that for $\alpha = 12^\circ$ (not shown in this paper).

Figure 4 shows the modifications of the force coefficients and drag polar by optimal strips for Re = 60 000 and 180 000. Without strip, discontinuity in the lift slope is observed near $\alpha = 3^\circ$ for both Reynolds numbers [5], indicating that laminar separation bubble exists at this angle of attack [32]. Abrupt stall caused by laminar separation bubble burst also occurs for both Reynolds numbers, resulting in lift decrease and drag increase after stall. The lift coefficients at low angles of attack for Re = 180 000 are similar to those for Re = 60 000, but the drag coefficients are lower at higher Reynolds number, which is consistent with the result of Selig *et al.* [5].

With optimal strips, the lift and drag coefficients at $\alpha = 12^\circ$ are increased by 31% and decreased by 35%, respectively, for Re = 60 000. The stall characteristics are also modified by the strips, i.e., from abrupt to broad stall, which suggests that flow-separation characteristics at these angles of attack are significantly changed by the strips. For Re = 180 000, the lift and drag coefficients at $\alpha = 13.5^\circ$ are increased by 12% and decreased by 40% with the strips, respectively, and the stall characteristics are also changed from abrupt to broad stall. It is noticeable that the drag coefficients in the broad stall region are larger at Re = 60 000 but smaller at Re = 180 000 than those without strip, while the lift and lift-to-drag ratio are significantly increased by the strips. This increase in the drag coefficient in the deep-stall region was also observed from the stall control by vortex generators [14].

Unlike in the broad stall region, the strips little change the lift and drag coefficients in the prestall region. This is because in the prestall region the flow is attached near the leading edge and laminar separation bubble forms near the trailing edge [32]. The height of the strips is smaller than the boundary layer thickness above the airfoil surface (e.g., $\delta/c \approx 0.004$ near the leading edge at $\alpha = 4^\circ$ for Re = 60 000 [32]) and thus the strips do not significantly modify the flow. Selig *et al.* [5] applied various trip wires to SD7003 airfoil and showed that the trip wires do not change the lift coefficient

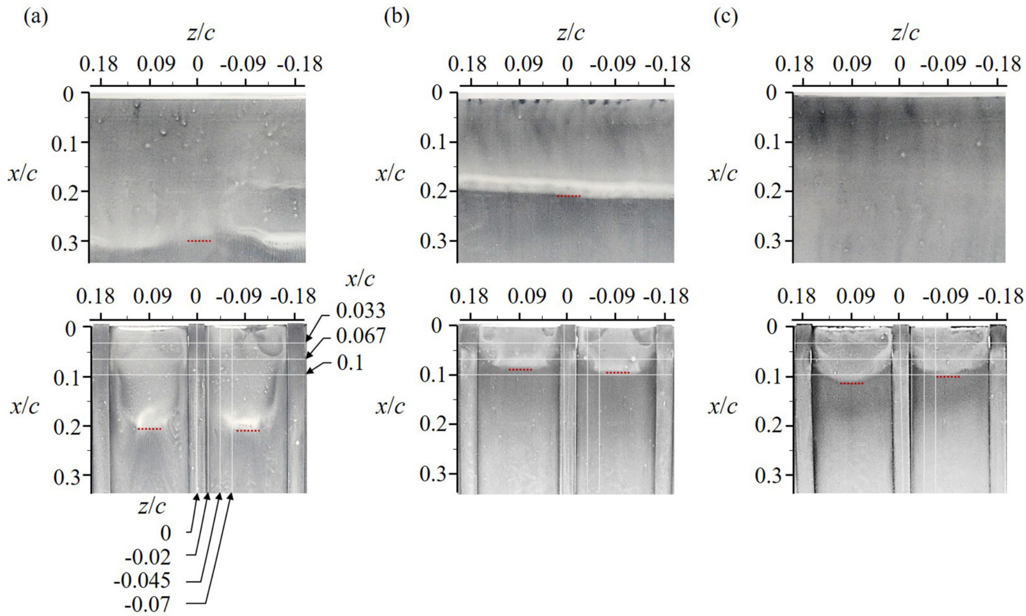

FIG. 5. Surface oil visualization on the suction surface (Re $= 60\,000$): (a) $\alpha = 9^\circ$ (prestall angle of attack); (b) $\alpha = 11^\circ$ (near-stall angle of attack); (c) $\alpha = 12^\circ$ (post-stall angle of attack). Here, the upper and lower panels denote the cases without and with strips, respectively. Red-dotted and white-solid lines denote the reattachment and PIV measurement locations, respectively.

at low angles of attack. Interestingly, the discontinuity observed in the lift coefficient near $\alpha = 3^\circ$ is eliminated by the strips at both Reynolds numbers. It suggests that the strips indeed modify laminar flow separation patterns at these low Reynolds numbers, but those modifications are not enough to significantly change the lift and drag forces.

The drag polar in Fig. 4(b) shows that the aerodynamic performance at high angles of attack is significantly improved by the strips, whereas there is small degradation in the aerodynamic performance at low angles of attack for low Reynolds number but the degradation disappears at higher Reynolds number. This suggests that the strips are a good high lift device.

B. Surface-oil visualization and velocity measurements on streamwise-vertical planes

Figure 5 shows the oil flow patterns on the suction surface with and without strip at $\alpha = 9^\circ$, 11°, and 12° corresponding to pre-, near-, and post-stall angles of attack, respectively. Without strip (upper panels in Fig. 5), flow separates from the leading edge and reattaches on the suction surface at $\alpha = 9^\circ$ and 11°, and the reattachment locations move upstream ($x/c = 0.3$ to 0.2) as the angle of attack increases. At a post-stall angle of attack ($\alpha = 12^\circ$), the flow does not reattach on the suction surface, resulting in an abrupt stall. However, with strips (lower panels in Fig. 5), flow separates from the leading edge in between the strips but reattaches near the center of grooved surface. The streamwise location of reattachment moves upstream with increasing angle of attack ($x/c = 0.2$ to 0.1 for $\alpha = 9^\circ$ to 11°), and is shorter than that without strip. At a post-stall angle of attack ($\alpha = 12^\circ$), the reattachment location does not move further upstream and is similar to that at $\alpha = 11^\circ$. Note also that flow remains fully attached above the strip for all angles of attack considered. The mean velocity fields at $\alpha = 12^\circ$ with and without strips are shown in Fig. 6. Without strip, flow fully separates from the leading edge. With strips, flow remains fully attached above the strip, and separates at the leading edge but reattaches at $x/c \approx 0.1$ above the grooved surface, which is consistent with the results from the surface-oil visualization.

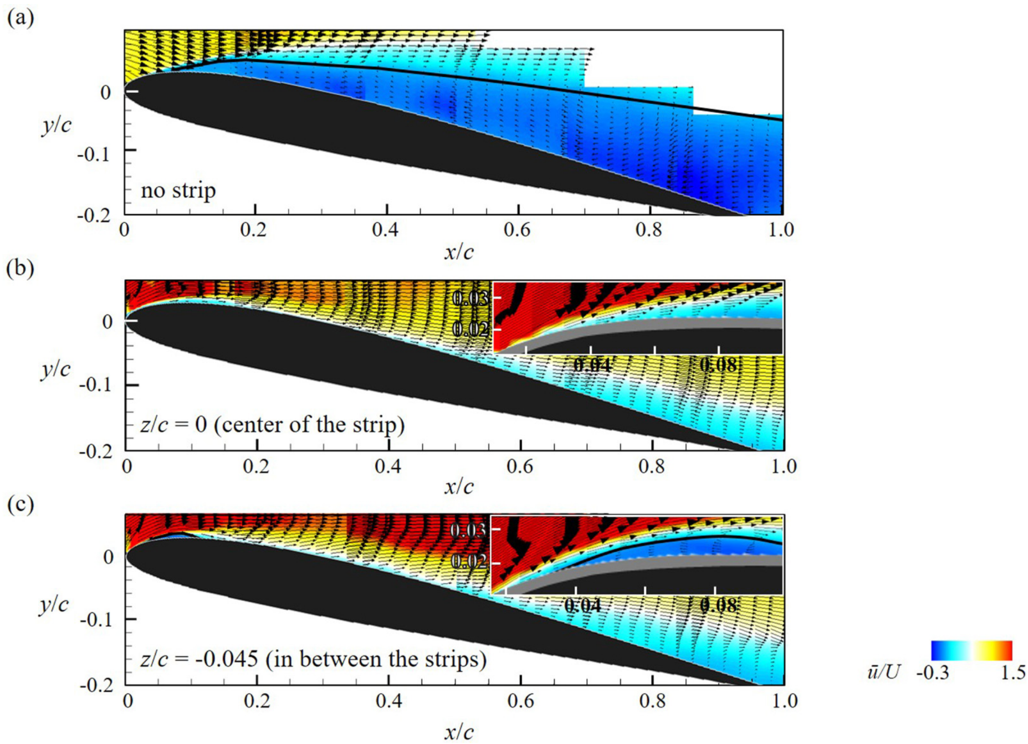

FIG. 6. Contours of mean streamwise velocity and velocity vectors ($\alpha = 12^\circ$; Re = 60 000): (a) no strip; (b) with strips (at $z/c = 0$); (c) with strips (at $z/c = -0.045$). Here, the thick black lines in (a) and (c) denote $\bar{\boldsymbol{u}} = 0$. Black- and gray-colored areas indicate the regions with no velocity measurement due to the shadows of the airfoil and strips, respectively.

Figure 7 shows the pressure distributions on the suction and pressure surfaces at $\alpha = 12^\circ$ with and without strips. The pressure coefficient on the suction surface is significantly changed by the strips. Its magnitude is much larger near the leading edge ($C_p \approx -3$) with strips than that without strip ($C_p \approx -1$). With strips, C_p on the grooved surface is nearly constant in the separated region ($x/c \leqslant 0.085$) except very near the leading edge, and then recovers downstream. However, the peak of $-C_p$ on the strip surface moves slightly downstream due to the fully attached flow and then the pressure recovers downstream. The pressures on the strip and grooved surfaces become similar at $x/c > 0.2$. These pressure distributions are also consistent with the results from surface oil flow visualization and mean velocity measurements. The pressure coefficient on the pressure surface with strips is insensitive to the spanwise location and is larger at $x/c < 0.2$ than that without strip, although its variation is less significant than that on the suction surface. Increase in the pressure coefficient on the pressure surface was also reported in previous studies [19,40].

C. Velocity measurements on cross-flow planes

Figure 8 shows the cross-flow velocity vectors above the suction surface very near the leading edge ($x/c = 0.033$) at $\alpha = 12^\circ$. At each corner of the strip, a streamwise vortex is generated whose diameter is comparable to the strip height, called corner vortex [41–47]. This corner vortex is manifest for both mean and instantaneous flows, although its strength is slightly reduced in the mean field. This corner vortex induces downwash motions very near the corner and to the strip surface, providing additional momentum and resulting in reattachment there [see also Figs. 5 and 6(b)]. The corner vortices are clearly a dominant flow structure at this streamwise location. It has been shown

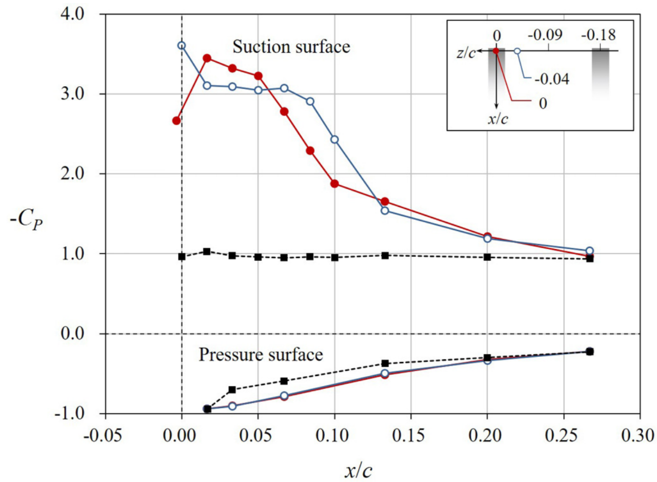

FIG. 7. Surface pressure distributions ($\alpha = 12°$; Re = 60 000): ■, no strip; ●, with strips ($z/c = 0$); ○, with strips ($z/c = -0.04$).

that a corner vortex is generated when flow passes through a corner with a streamwise curvature [42,47], and is observed in various conditions such as wing-body [41,43] or turbine (compressor) blade-hub junctions [44–46]. It has been also shown that the corner vortex starts from the corner and travels away from the corner in the spanwise direction as it moves downstream [47]. We will show below that this observation is consistent with the spanwise movement of the present corner vortex.

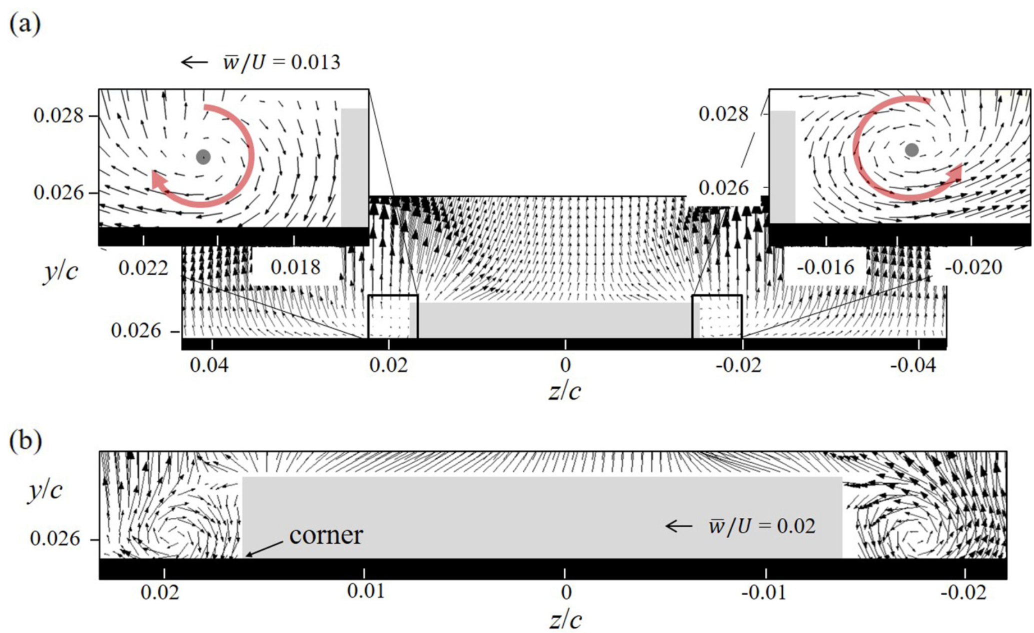

FIG. 8. Cross-flow velocity vectors at $x/c = 0.033$ ($\alpha = 12°$; Re = 60 000): (a) mean field; (b) instantaneous field. Here, the laser sheet for PIV is nearly perpendicular to the airfoil surface.

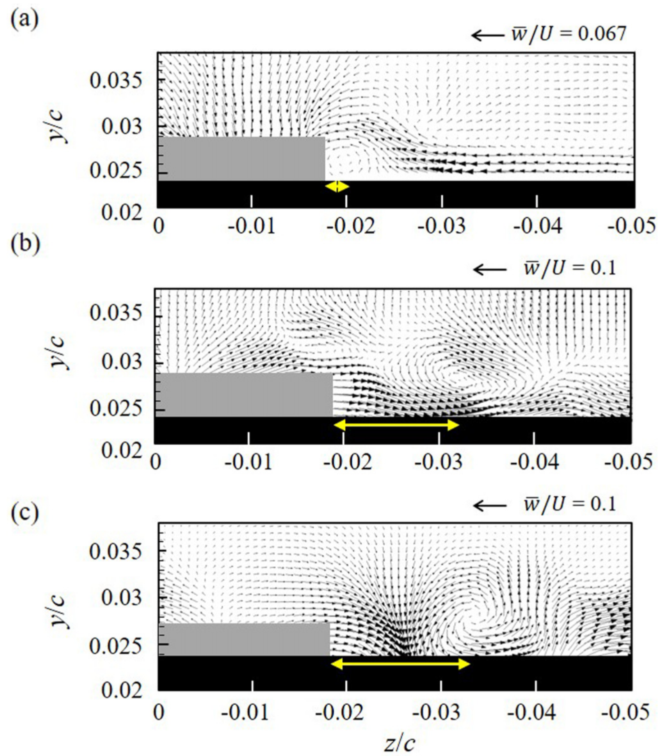

FIG. 9. Instantaneous cross-flow velocity vectors ($\alpha = 12^\circ$; Re = 60 000): (a) $x/c = 0.05$; (b) 0.067; (c) 0.1. Black- and gray-colored areas in this figure denote the regions of no velocity measurement due to the shadows of the airfoil and strips, respectively. Yellow arrows denote the locations of corner vortex center from the strip corner.

Figure 9 shows the instantaneous cross-flow velocity vectors at $x/c = 0.05$, 0.067, and 0.1 at $\alpha = 12^\circ$. The strength of corner vortices significantly increases at these streamwise locations [compare them with corner vortices at $x/c = 0.033$ in Fig. 8(b)]. The direction of the spanwise velocity very near the grooved surface is consistent with the spanwise pressure gradient formed in this region (see Fig. 7 and below). Figure 10 shows the locations of corner vortex center obtained from the mean cross-flow fields at four different streamwise locations ($x/c = 0.033,\ 0.05,\ 0.067$, and 0.1), together with surface-oil flow pattern on the suction surface at $\alpha = 12^\circ$. The corner vortex stays very near the corner until $x/c \leqslant 0.05$ and then moves toward the center of grooved surface while moving downstream. These vortices provide additional momentum near the corners and thus the reattachment starts from the corner and moves away from the corner. This movement of the corner vortices is consistent with the spanwise pressure gradient formed there: i.e., at $0.0167 \leqslant x/c \leqslant 0.05$, the pressure at $z/c = -0.04$ is higher than that at $z/c = 0$ and thus $\partial P/\partial z < 0$ there (Fig. 7), forcing the corner vortex to stay near the corner, whereas $\partial P/\partial z > 0$ at $0.05 < x/c < 0.133$, which pushes the corner vortex away from the corner. With this movement of corner vortex, the reattachment starts from the corner and move to the center of grooved surface (Fig. 10). A similar movement of corner vortices was observed from the junction flow between a turbine blade and end-wall [47].

Figure 11 shows the contours of the Reynolds shear stress at $z/c = 0$, -0.02, -0.045, and -0.07 with strips at $\alpha = 12^\circ$. The criterion to determine laminar to turbulent transition is set to be $-\overline{u'v'}/U^2 \geqslant 0.001$ [48]. At $z/c = 0$ (above strip surface) where flow is fully attached, transition

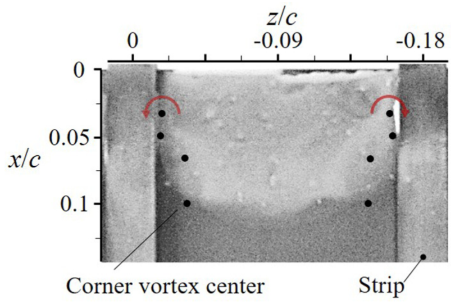

FIG. 10. Locations of corner vortex center in the streamwise direction and surface-oil flow pattern on the suction surface ($\alpha = 12^\circ$; Re = 60 000). Here, vortex-center locations are obtained from the mean cross-flow fields at $x/c = 0.033$, 0.05, 0.067, and 0.1. Black dots and red arrows indicate the locations and rotational directions of corner vortices, respectively.

occurs near $x/c = 0.05$. At $z/c = -0.02$ (near the strip edge), transition also occurs near $x/c = 0.05$. Transition occurs further downstream as the spanwise distance from the strip edge increases. At $z/c = -0.07$ (near the center of the grooved surface between the strips), reattachment occurs at $x/c = 0.1$ [Fig. 5(c)] and transition occurs a little upstream of the reattachment ($x/c \approx 0.09$). That is, reattachment occurs due to additional momentum supply by laminar to turbulence transition along the separating shear layer.

The mechanism responsible for the aerodynamic performance enhancement by the strips is plotted in Fig. 12. Without strip, an overall separation occurs from the leading edge at the post-stall angle of attack of 12°. With strips, corner vortices evolve from the corners of strips and induce downwash motion on and near the strip surface, resulting in attached flow there. As the corner vortices travel downstream, they move away from the corners of the strips in the spanwise direction

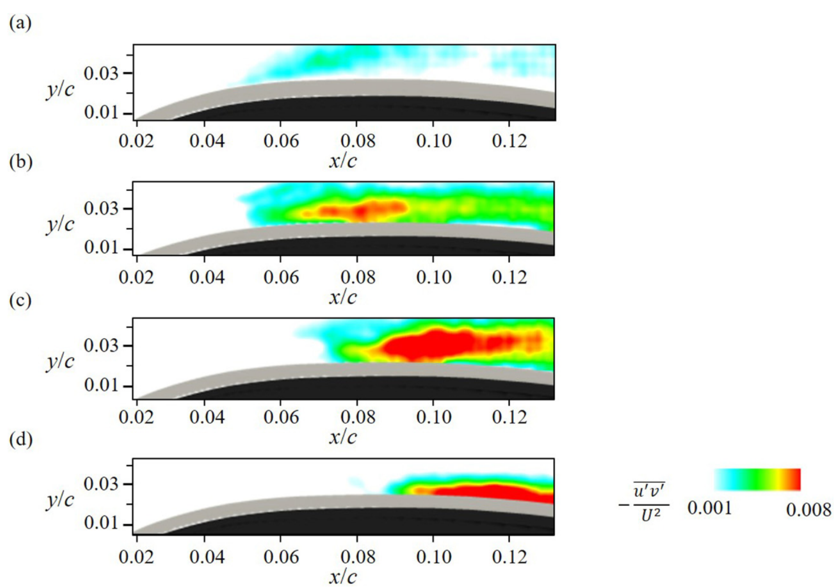

FIG. 11. Contours of the Reynolds shear stress with strips ($\alpha = 12^\circ$; Re = 60 000): (a) $z/c = 0$; (b) -0.02; (c) -0.045; (d) -0.07.

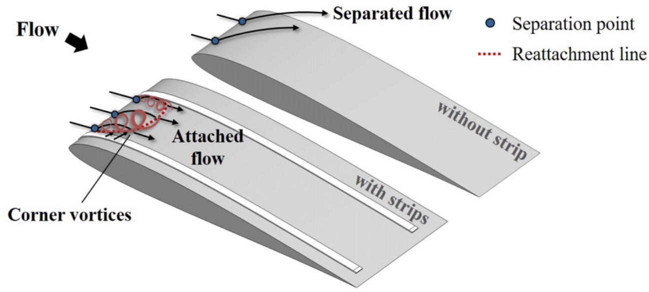

FIG. 12. Schematic diagram of the mechanism responsible for the lift increase by the strips at a post-stall angle of attack.

and thus provide downwash motion on wider area, reattaching flow on the whole spanwise domain at $x/c = 0.1$ with additional mixing from turbulence evolution along the separated shear layer.

D. Effect of the strip length on the drag and lift forces

So far, we have considered the case where the strips are installed on most of airfoil surface in the streamwise direction [Fig. 1(b)], where the streamwise length of strips is $l = 0.97c$. Figure 13 shows the effects of the streamwise strip length on the force coefficients. Here, we change the length of the strips only on the suction surface without changing the strip length on the pressure surface: $l/c = 0, 0.033,\ 0.1, 0.67$, and 0.97. First, the strips located only on the pressure surface (the case of $l/c = 0$) little change the force coefficients for all angles of attack, indicating that the strips there do not play any meaningful role. In the prestall region, the drag and lift coefficients are not much changed by the strips, but the discontinuity in the lift coefficient at $\alpha = 3^\circ$ disappears for the strip length of $l/c \geqslant 0.67$. This indicates that strips with $l/c \geqslant 0.67$ can control laminar separation bubble because it is formed in mid chord ($x/c \approx 0.5$) at low angles of attack [32] and cannot be controlled by shorter

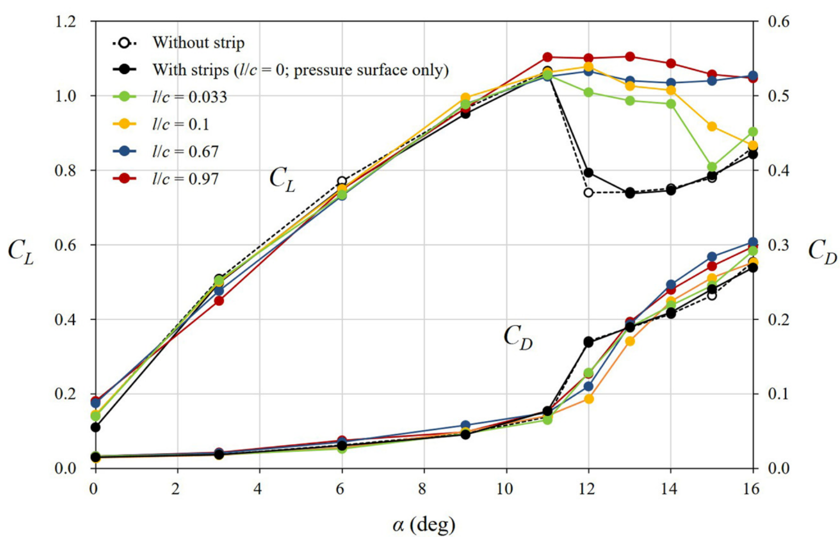

FIG. 13. Variations of the force coefficients (C_L and C_D) with the strip length (l) on the suction surface (Re = 60 000). Here, other strip parameters are fixed to be $h/c = 0.003,\ w/c = 0.03$, and $s/c = 0.15$, and the strip length on the pressure surface is fixed at $l/c = 0.97$.

strips ($l/c \leqslant 0.5$). In post-stall region, with increasing strip length, the lift coefficient increases more, and the range of broad stall gets broader. The drag coefficient with strips is lower at $11^\circ < \alpha \leqslant 13^\circ$ and higher at $\alpha > 13^\circ$ than that without strip. The aerodynamic performance (lift-to-drag ratio) in the post-stall region is significantly improved when the strip length approaches the chord length.

IV. CONCLUSIONS

In this study, we suggested longitudinal strips as a new device for stall control of low Reynolds number airfoils. We applied the strips on nearly whole surface of SD7003 airfoil at Re = 60 000 and 180 000, and obtained optimal configuration of strips (height, width and spacing) at a post stall angle of attack ($\alpha = 12^\circ$) using a response surface method. The optimal strips significantly increased the aerodynamic performance in the post-stall region and changed the abrupt stall to broad stall, whereas they little reduced the aerodynamic performance in the prestall region. To identify the mechanisms responsible for the changes in the force coefficients, flow visualization, and surface pressure and flow field measurements were conducted at $\alpha = 12^\circ$. A dominant flow structure with strips was the corner vortices. Clockwise and counterclockwise streamwise vortices were generated at the left- and right-facing corners near the leading edge, respectively, and they slowly moved away from the corners while travelling downstream. These vortices provided additional momentum to the airfoil surface, resulting in fully attached flow above the strips and reattachment of flow above grooved surface. The force coefficients were not changed by very short strips located near the leading edge, but the lift coefficient (or lift-to-drag ratio) increased more with longer strips in the post-stall region, showing an importance of locating the strips over the entire surface of the airfoil.

Conventional stall-control devices have limitations at off-design conditions. For example, vortex generators designed for stall control increase drag at low angles of attack [12,14,15], or those for decreasing drag at low angles of attack have no stall control effect [13]. Trip wires and zigzag tapes reduced drag at low angles of attack but did not function as a stall control device [16–18,22,23]. Burst control plate controlled stall, but reduced and increased the lift and drag, respectively, at low angles of attack [20]. These devices were installed along the spanwise direction in a limited streamwise domain. The longitudinal strips presented here are different from these devices, in that the strips are installed on nearly the whole airfoil surface but with low heights less than the boundary layer thickness and produce positive control effects at post-stall angles of attack but little affect the aerodynamic performance at prestall angles of attack. Therefore, the longitudinal strip is expected to be a new stall-control device which improves the aerodynamic performance of low Reynolds number airfoils at high angles of attack.

ACKNOWLEDGMENT

This research was supported by the research program of National Research Foundation, Korea (Grant No. NRF-2016R1E1A1A02921549).

[1] R. Austin, *Unmanned Aircraft Systems: UAVs Design, Development and Deployment* (Wiley, Reston, 2010), p. 5.
[2] T. J. Mueller and J. D. DeLaurier, Aerodynamics of small vehicles, Annu. Rev. Fluid Mech. **35**, 89 (2003).
[3] P. B. S. Lissaman, Low-Reynolds-number airfoils, Annu. Rev. Fluid Mech. **15**, 223 (1983).
[4] M. Gad-el-Hak, Control of low-speed airfoil aerodynamics, AIAA J. **28**, 1537 (1990).
[5] M. S. Selig, J. F. Donovan, and D. B. Fraser, *Airfoils at Low Speeds* (HA Stokely, Virginia, 1989).
[6] M. Gad-el-Hak, *Flow Control: Passive, Active, and Reactive Flow Management* (Cambridge University Press, New York, 2000), p. 150.

[7] R. Sosa, G. Artana, E. Moreau, and G. Touchard, Stall control at high angle of attack with plasma sheet actuators, Exp. Fluids **42**, 143 (2007).

[8] D. Greenblatt, T. Schneider, and C. Y. Schüle, Mechanism of flow separation control using plasma actuation, Phys. Fluids **24**, 077102 (2012).

[9] M. Sato, T. Nonomura, K. Okada, K. Asada, H. Aono, A. Yakeno, Y. Abe, and K. Fujii, Mechanisms for laminar separated-flow control using dielectric-barrier-discharge plasma actuator at low Reynolds number, Phys. Fluids **27**, 117101 (2015).

[10] K. B. M. Q. Zaman, Effect of acoustic excitation on stalled flows over an airfoil, AIAA J. **30**, 1492 (1992).

[11] A. Bar-Sever, Separation control on an airfoil by periodic forcing, AIAA J. **27**, 820 (1989).

[12] J. D. Nickerson Jr., A study of vortex generators at low Reynolds numbers, in *24th Aerospace Sciences Meeting, Reno, NV* (AIAA, Reston, VA, 1986), AIAA Paper No. 1986–0155.

[13] M. Kerho, S. Hutcherson, R. F. Blackwelder, and R. H. Liebeck, Vortex generators used to control laminar separation bubbles, J. Aircraft **30**, 315 (1993).

[14] J. S. Delnero, J. M. Di Leo, M. E. Camocardi, M. A. Martinez, and J. L. Colman-Lerner, Experimental study of vortex generators effects on low Reynolds number airfoils in turbulent flow, Int. J. Aerodynamics **2**, 50 (2012).

[15] H. Tebbiche and M. S. Boutoudj, Optimized vortex generators in the flow separation control around a NACA0015 profile, in *Proceedings of the 9th International Conference on Structural Dynamics, Porto, Portugal, 2014*, edited by Á. Cunha, E. Caetano, P. Ribeiro, and G. Müller, pp. 3219–3226, https://paginas.fe.up.pt/~eurodyn2014/CD/papers/449_MS20_ABS_1618.pdf.

[16] A. F. Huber II and T. J. Mueller, The effect of trip wire roughness on the performance of the Wortmann FX 63–137 airfoil at low Reynolds numbers, Exp. Fluids **5**, 263 (1987).

[17] C. A. Lyon, M. S. Selig, and A. P. Broeren, Boundary layer trips on airfoils at low Reynolds numbers, in *Proceedings of the 35th Aerospace Sciences Meeting & Exhibit, Reno, Nevada* (AIAA, Reston, VA, 1997), AIAA Paper No. 1997–0511.

[18] L. W. Traub, Experimental investigation of the effect of trip strips at low Reynolds number, J. Aircraft **48**, 1776 (2011).

[19] K. Rinoie, M. Okuno, and Y. Sunada, Airfoil stall suppression by use of a bubble burst control plate, AIAA J. **47**, 322 (2009).

[20] C. W. Wong and K. Rinoie, Bubble burst control for stall suppression on a NACA 63_1-012 airfoil, J. Aircraft **46**, 1465 (2009).

[21] Y. Nakamura, K. Rinoie, and Y. Sunada, Airfoil stall suppression by use of rectangular cross-section burst control plates, in *Proceedings of the 50th Aerospace Sciences Meeting Including the New Horizons Forum and Aerospace Exposition, Nashville, Tennessee* (AIAA, Reston, VA, 2012), AIAA Paper No. 2012–0318.

[22] M. S. Selig and B. D. McGranahan, Wind tunnel aerodynamic tests of six airfoils for use on small wind turbines, J. Solar Energy Engng. **126**, 986 (2004).

[23] S. Mack, C. Brehm, B. Heine, A. Kurz, and H. F. Fasel, Experimental investigation of separation and separation control on a laminar airfoil, in *Proceedings of the 4th Flow Control Conference, Seattle, Washington* (AIAA, Reston, VA, 2008), AIAA Paper No. 2008–3766.

[24] K. Tongsawang and M. P. Thesis, The University of Sheffield, Sheffield, 2015.

[25] J. C. Lin, Review of research on low-profile vortex generators to control boundary-layer separation, Progr. Aerospace Sci. **38**, 389 (2002).

[26] J. B. Barlow, W. H. Rae, Jr., and A. Pope, *Low-speed Wind Tunnel Testing* (Wiley, New York, 1999) p. 349.

[27] T. J. Mueller and T. F. Burns, Experimental studies of the Eppler 61 airfoil at low Reynolds numbers, in *Proceedings of the 20th Aerospace Sciences Meeting, Orlando, Florida* (AIAA, Reston, VA, 1982), AIAA paper No. 1982–0345.

[28] M. S. H. Boutilier and S. Yarusevych, Effects of end plates and blockage on low-Reynolds-number flows over airfoils, AIAA J. **50**, 1547 (2012).

[29] A. A. Giunta, Ph.D. thesis, Virginia Polytechnic Institute and State University, Virginia, 1997.

[30] R. H. Myers and D. C. Montgomery, *Response Surface Methodology: Process and Product Optimization Using Designed Experiments* (John Wiley & Sons, New York, 2002) p. 219.

[31] B. Mohammadi and O. Pironneau, Shape optimization in fluid mechanics, Annu. Rev. Fluid Mech. **36**, 255 (2004).

[32] M. C. Galbraith and M. R. Visbal, Implicit large eddy simulation of low-Reynolds-number transitional flow past the SD7003 airfoil, in *Proceedings of the 40th Fluid Dynamics Conference and Exhibit, Chicago, Illinois* (AIAA, Reston, VA, 2010), AIAA paper No. 2010–4737.

[33] J. M. Caram and A. Ahmed, Effect of Ribblets on turbulence in the wake of an airfoil, AIAA **29**, 1769 (1991).

[34] S. J. Lee and Y. G. Jang, Control of flow around a NACA 0012 airfoil with a micro-riblet film, J. Fluids Structures **20**, 659 (2005).

[35] M. J. Werle, R. W. Paterson, and W. M. Presz Jr., Trailing-edge separation/stall alleviation, AIAA **25**, 624 (1987).

[36] H. W. Coleman and W. G. Steele, *Experimentation, Validation, and Uncertainty Analysis for Engineers* (John Wiley & Sons, New York, 2009).

[37] M. S. Selig, J. J. Guglielmo, A. P. Broeren, and P. Giguère, *Summary of Low Speed Airfoil Data* (SoarTech Publications, Virginia, 1995).

[38] D. P. Hart, Super-resolution PIV by recursive local-correlation, J. Visual. **3**, 187 (2000).

[39] J. Westerweel and F. Scarano, Universal outlier detection for PIV data, Exp. Fluids **39**, 1096 (2005).

[40] N. Rostamzadeh, K. L. Hansen, R. M. Kelso, and B. B. Dally, The formation mechanism and impact of streamwise vortices on NACA 0021 airfoil's performance with undulating leading edge modification, Phys. Fluids **26**, 107101 (2014).

[41] I. M. M. A. Shabaka and P. Bradshaw, Turbulent flow measurements in an idealized wing/body Junction, AIAA J. **19**, 131 (1981).

[42] X. Yu, Z. Zhang, and B. Liu, The evolution of the flow topologies of 3D separations in the stator passage of an axial compressor stage, Exp. Thermal Fluid Sci. **44**, 301 (2013).

[43] F. Gand, J. C. Monnier, J. M. Deluc, and A. Choffat, Experimental study of the corner flow separation on a simplified junction, AIAA J. **53**, 2869 (2015).

[44] H. P. Wang, S. J. Olson, R. J. Goldstein, and E. R. G. Eckert, Flow visualization in a linear turbine cascade of high performance turbine blades, J. Turbomach. **119**, 1 (1997).

[45] L. Langston, Secondary flows in axial turbines—A review, Ann. NY Acad. Sci. **934**, 11 (2001).

[46] H. Zhang, S. Wang, and Z. Wang, Variation of vortex structure in a compressor cascade at different incidences, J. Propul. Power **23**, 221 (2007).

[47] M. Y. Jabbari, R. J. Goldstein, K. C. Marston, and E. R. G. Eckert, Three dimensional flow at the junction between a turbine blade and end-wall, Wärme-und Stoffübertragung **27**, 51 (1992).

[48] R. Hain, C. J. Kähler, and R. Radespiel, Dynamics of laminar separation bubbles at low-Reynolds-number aerofoils, J. Fluid Mech. **630**, 129 (2009).